applied sciences

MDPI

Article

Evaluating Tissue Mechanical Properties Using Quantitative Mueller Matrix Polarimetry and Neural Network

Changjiang Mi [1,†], Conghui Shao [1,2,†], Honghui He [1,*], Chao He [3,*] and Hui Ma [1,2]

[1] Guangdong Research Center of Polarization Imaging and Measurement Engineering Technology, Shenzhen Key Laboratory for Minimal Invasive Medical Technologies, Institute of Biopharmaceutical and Health Engineering, Tsinghua Shenzhen International Graduate School, Tsinghua University, Shenzhen 518055, China
[2] Department of Physics, Tsinghua University, Beijing 100084, China
[3] Department of Engineering Science, University of Oxford, Parks Road, Oxford OX1 3PJ, UK
* Correspondence: he.honghui@sz.tsinghua.edu.cn (H.H.); chao.he@eng.ox.ac.uk (C.H.)
† These authors contributed equally to this work.

Abstract: Evaluation of the mechanical properties of biological tissues has always been an important issue in the field of biomedicine. The traditional method for mechanical properties measurement is to perform in vitro tissue deformation experiments. With the fast development of optical and image processing techniques, more and more non-invasive and non-contact optical methods have been applied to the analysis of tissue mechanical features. In this study, we use Mueller matrix polarimetry to quantitatively obtain the mechanical properties of bovine tendon tissues. Firstly, to study the structural information and the changes in the optical characteristics of the tendon tissue under different stretching states, 3×3 Mueller matrix images of bovine tendon tissue samples are acquired by backscattering measurement setups based on a polarized camera. Then, we extract the frequency distribution histograms (FDHs) of the Mueller matrix elements to reveal the structural changes of the tendon tissue more clearly during the stretching process. Last, we calculate the Mueller matrix transformation (MMT) parameters, the total anisotropy t_1 and the anisotropy direction α_1 of the tendon tissue samples under different stretching processes to quantitatively characterize their structural changes under different mechanical states. The central moments of the MMT parameters can be used to distinguish the different stretching states of the tendon tissue. For better discrimination based on the MMT parameters, we design a multilayer neural network that takes the first-order moments of the MMT parameters as the input features. After training, a high-precision classification model of the stretching states of tendon tissue samples is finally obtained, and the total classification accuracy achieves 98%. The experimental results show that the Mueller matrix polarimetry can be a potential non-contact tool for tissue mechanical properties evaluation.

Keywords: mechanical property; polarimetry; Mueller matrix; tissue; neural network

Citation: Mi, C.; Shao, C.; He, H.; He, C.; Ma, H. Evaluating Tissue Mechanical Properties Using Quantitative Mueller Matrix Polarimetry and Neural Network. *Appl. Sci.* **2022**, *12*, 9774. https://doi.org/10.3390/app12199774

Academic Editors: Amerigo Capria and Santiago Royo

Received: 22 August 2022
Accepted: 23 September 2022
Published: 28 September 2022

1. Introduction

Evaluating the mechanical properties of biological tissues has always been an important issue in the field of biomedicine. Biological tissues vary widely in morphology, structure, and function and have characteristics such as heterogeneity, anisotropy, and viscoelasticity [1,2]. In addition, the morphology, structure, production and development, lesions, and even death of organisms are related to mechanical properties [3]. For tissues, their mechanical properties mainly include elastic modulus, yield strength, ultimate strength and so on [4]. The most direct way to detect these properties is to measure the deformation of tissue when it is disturbed. The traditional detection method is mainly to carry out in vitro or invasive tissue deformation experiments [5]. Currently, the available methods include digital image correlation (DIC), the basic idea of which is to obtain a continuous speckled image of the object before and after deformation, and then use image recognition processing technology to obtain changes in the digital gray field to measure

mechanical parameters such as displacement and strain [6], which is a method of obtaining object performance parameters based on the natural or artificial spotting field of the surface before and after deformation. Optical coherence elastography (OCE) can measure tissue deformation due to excitation and accurately obtain tissue elastic information [7]. Ultrasound elastography and MRI [8] can obtain tissue strain and strain rate, but with limited resolution. With the fast development of optical and image processing techniques, more and more non-invasive and non-contact optical methods have been applied to the analysis of tissue mechanical features.

In the past decade, Mueller matrix polarimetry is gaining more and more attention in biomedical studies and applications [9]. Compared with non-polarized optical methods, Mueller matrix polarimetry is sensitive to microstructures and can additionally provide information on the optical anisotropy of tissues, including birefringence and linear dichroism (LD), noninvasively [9,10]. At present, the commonly used Mueller matrix measurement method is based on the dual-rotating retarders method proposed by Azzam [11], which can eliminate the image deformation induced by the rotation of the polarizers. Moreover, there are also Mueller matrix measurement methods based on polarization cameras to improve the measurement efficiency for dynamic biomedical samples [12]. In this work, we use Mueller matrix polarimetry to quantitatively detect and evaluate the mechanical properties of tendon tissues stretched by different external forces. Firstly, we measure the 3×3 Mueller matrix images of bovine tendon tissue samples with different stretching states using the backscattering measurement setups based on a polarization camera. Then, we extract the frequency distribution histograms (FDHs) of the Mueller matrix elements to reveal the structural changes of the tendon tissue during the stretching process. Last, for the quantitative characterization of their structural changes, we calculate the Mueller matrix transformation (MMT) parameters of the tendon tissue samples under different stretching states. We also design a multilayer neural network for better discrimination based on the MMT parameters. A high-precision classification model with an accuracy of 98% for the stretching states of tendon tissue samples is finally obtained. It is demonstrated that Mueller matrix polarimetry can be a potential non-contact tool for the evaluation of tissue mechanical properties.

2. Materials and Methods

2.1. Experimental Setup and Tendon Tissue Samples

In this work, a polarized camera-based (Dofp PHX050S-P, Lucid Vision Labs, Richmond, BC, Canada) backscattering measurement device was used to obtain the 3×3 Mueller matrix images of the samples. Each pixel of the polarization camera is covered with four miniature polarizers along 0, 45, 90 and 135 deg to detect four SOPs at the same time. Thus, the raw image acquired by the polarization camera can be divided into four images, recording the light intensity data of 0, 45, 90 and 135 deg of linearly polarized light, respectively. Then the first three components of the Stokes vector S1, S2 and S3 can be calculated accordingly [13]. To obtain the complete 3×3 Mueller matrix, incident light with three states of polarization (SOP) of 0 deg, 45 deg and 90 deg were used.

As shown in Figure 1a, the incident light emitted from an LED (3 W, 633 nm, Daheng Optic, Beijing, China) passes through the lens L1(LBTEK Optic, Changsha, China), and the rotatable polarizer (P1, extinction ratio >1000:1, LBTEK Optic, Changsha, China) becomes linearly polarized light with different SOPs. The photons scattered from the sample are detected by the polarization camera (Dofp PHX050S-P, Lucid Vision Labs, Vancouver, Canada) after passing through the lens L2 (LBTEK Optic, Changsha, China). To avoid the influence of sample surface reflection, there is an oblique incident angle (θ) of 7 deg between the incident light arm and the detection arm. Before the measurements, the Mueller matrix imaging system was calibrated using several standard samples, including air, polarizers, fibrous scatterers and retarders in both transmission and backscattering modes. The results showed that the maximum error of the individual Mueller matrix elements is about 0.8%. More details of the calibration process can be found in Ref. [14].

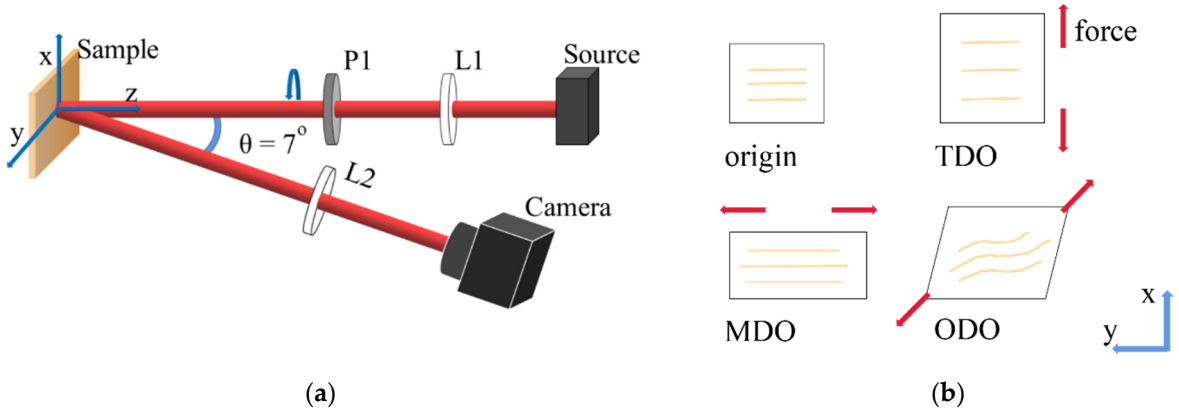

Figure 1. (**a**) Schematic of the experimental setup for the backscattering Mueller matrix measurement. P1: polarizer; L1, L2: lens. The oblique incident angle θ is about 7 deg to avoid the surface reflection from the sample. The diameter of the illumination area is about 2.3 cm. (**b**) Schematic diagram of four stretching states of tendon tissue samples: origin means unstretched, TDO means transverse stretched, MDO means longitudinal stretched and ODO means 45 deg stretched. The light orange lines represent the fibers.

Tendon tissues are highly anisotropic, resulting from both optical birefringence and scattering of fibrous structures [15]. There are abundant collagen fibers in tendon tissues, and most of them are arranged in the same direction [16]. Previously, it has been demonstrated that information on fibrous structures in tendon tissues, such as their density and orientation, can be obtained from the Mueller matrix [17]. However, applying an external force on tendon tissues will lead to changes in their mechanical features and anisotropic properties [18]. Here, to study the ability of Mueller matrix derived parameters to evaluate the mechanical properties of tendon tissues when stretched by external forces at different orientations, we measure fresh bovine tendon tissue samples sequentially at different physiological states as Figure 1b shows: without stretching (origin), transverse stretching (TDO), longitudinal stretching (MDO) and 45 deg stretching (ODO). Bovine tendon tissue with no external force is called the origin state sample, whose length and width are both 4.5 cm and the thickness is 0.5 cm. We stretched the tendon tissue 1 cm perpendicular to the alignment direction of the original collagen fibers, and this tissue is called the transverse stretching (TDO) state sample. Then, the restored tendon tissue was stretched 1 cm along the alignment direction of the original collagen fibers, and this tissue is called the longitudinal stretching (MDO) state sample. Last, we stretched the restored tendon tissue 1 cm along the 45 deg direction with the alignment of the original collagen fibers, and this tissue is called the 45 deg stretching (ODO) state sample. For each sample, a total of four 3×3 Mueller matrix images in different states are recorded for further analysis.

2.2. Frequency Distribution Histograms and Mueller Matrix Transformation Parameters

Among the available polarization imaging methods, Mueller matrix polarimetry has some unique advantages for tissue measurement. As a label-free and non-contact technique, Mueller matrix polarimetry is sensitive to the changes in subwavelength micro-structures and contains rich optical information of the samples, which have shown great application prospects in biomedical studies recently [19]. For bulk tendon tissues whose light scattering property is prominent, the 3×3 Mueller matrix can be used to conveniently obtain most of the structural information [20]. The 3×3 Mueller matrix is calculated by analyzing the relationship between the SOPs of scattered light and the incident light as shown in Equation (1):

$$S_{\text{out}} = M_{\text{sample}} \times S_{\text{in}} = \begin{bmatrix} M11 & M12 & M13 \\ M21 & M22 & M23 \\ M31 & M32 & M33 \end{bmatrix} \times S_{\text{in}} \quad (1)$$

where S_{in} represents the Stokes vector of the incident light, S_{out} represents the Stokes vector of scattered light, and M_{sample} represents the Mueller matrix of the sample.

The backscattered 3 × 3 Mueller matrix images of the bovine tendon tissue samples in different states are shown in Figure 2, from which we can clearly notice that the change in applied external force affects each matrix element differently, benefiting us in the qualitative collection and evaluation of the microstructural information related to the mechanical properties of the tissue. For instance, in the M12, M21, M13 and M31 elements, the linear dichroism induced by the tissue fibers is recorded; the values of diagonal elements M22 and M33 reflect the linear depolarization ability of the tissue; and the differences between the M22, M33, M23 and M32 elements reveal the total anisotropy of the tissue [9,21,22]. However, though the 2D Mueller matrix images contain abundant tissue microstructure information, it is difficult to find a direct and quantitative connection between a certain microstructure and the Mueller matrix elements [12,23]. To solve this problem, here we adopt the frequency distribution histogram (FDH) processing on the individual Mueller matrix elements to calculate their central moments [24]. Furthermore, we combine the Mueller matrix transformation (MMT) parameters and neural network (NN) to quantitatively evaluate the tendon tissues with different mechanical properties.

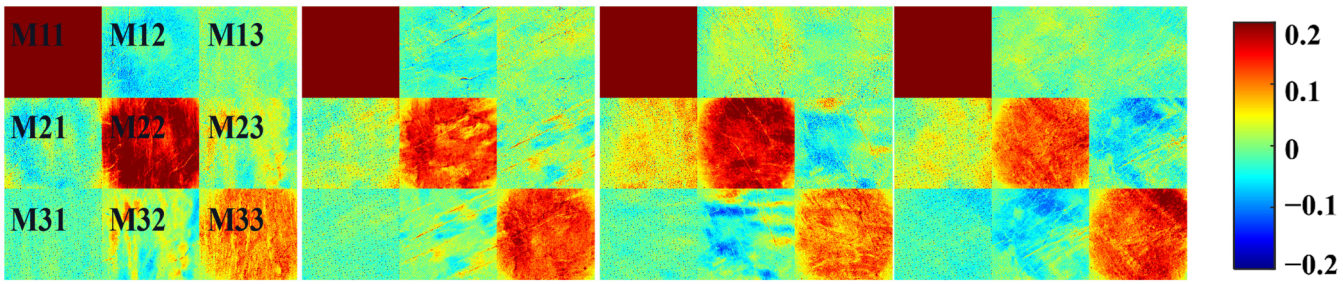

Figure 2. Two-dimensional (2D) backscattering 3 × 3 Mueller matrix images of bovine tendon tissue samples: (**a**) without stretching (origin), (**b**) transverse stretching (TDO), (**c**) longitudinal stretching (MDO), and (**d**) 45 deg stretching (ODO). All the Mueller matrix elements are normalized by the M11. The color bar is from −1 to 1 for the M11, −0.2 to 0.2 for the M22 and M33 and from −0.1 to 0.1 for other elements. It should be noted that the self-normalized M11 is polarization irrelevant.

Equations (2) and (3) define two MMT parameters used in this study: t_1 is a rotation invariant to characterize the total anisotropy induced by both dichroism and birefringence of the sample, while α_1 represents the orientation of the general anisotropy [21,25]. For bulk tissue samples with prominent fibrous structures, it was found that the statistical information of the MMT parameters α_1 and t_1 have the potential to detect external forces applied to the sample at different angles.

$$t_1 = \frac{1}{2}\sqrt{(M22 - M33)^2 + (M23 + M32)^2} \tag{2}$$

$$\alpha_1 = \frac{1}{4}atan2(M23 + M32, M22 - M33) \quad if \ \ t_1 \neq 0 \tag{3}$$

2.3. Central Moments

For further quantitative analysis, we calculate the central moments of the FDHs for the MMT parameters to see their statistical differences [24]. Suppose we have a random variable X whose central moments, expected value (I_1), variance (I_2), skewness (I_3), and kurtosis (I_4), are given as Equations (4)–(7), where σ represents the standard deviation of X and μ represents the mean of X:

$$I_1 = \mathrm{E}(X) \tag{4}$$

$$I_2 = \mathrm{Var}(X) \tag{5}$$

$$I_3 = \frac{\mathrm{E}(X-\mu)^3}{\sigma^3} \tag{6}$$

$$I_4 = \frac{\mathrm{E}(X-\mu)^4}{\sigma^4} \tag{7}$$

By observing the central moments values, we can quantitatively characterize a distribution curve. Here, I_1 is the mean value of the distribution curve, representing the mathematical expectation of the distribution; I_2 is the variance of the distribution, representing the degree of dispersion; I_3 represents the skewness of the distribution curve, which is a measure of the direction and degree of the skewed distribution of the statistical data, as well as a mathematical feature of the degree of asymmetry; I_4 represents the kurtosis of the distribution curve, which is the number of features characterizing the peak of the probability density distribution curve. Intuitively, the kurtosis reflects the thickness of the tail of the distribution curve. The detailed physical interpretations of the central moments can be found in Refs. [26,27]. In this study, we first record the 2D backscattering Mueller matrix images of the tendon tissue samples, then transfer the pixels of Mueller matrix elements and MMT parameters to FDHs by statistical analysis. Finally, the central moments of the FDHs are obtained according to Equations (4)–(7).

2.4. Neural Networks

An artificial neural network (ANN), or neural network (NN) for short, is a mathematical or computational model that mimics the structure and function of biological neural networks [28]. NNs are made up of many human–neural connections that adaptively change internal node parameters based on input characteristics. Modern NNs are nonlinear statistical data modeling tools that are often used to model complex relationships between inputs and outputs or to explore patterns in data [29].

Dense neural networks (DNNs) consist of connected layers of artificial neurons. All the nodes in each layer are connected to all the nodes in the neighboring layers (fully connected network, also referred to in the literature as a feed-forward NN or multilayer-perceptron-based networks [30]. Usually, DNNs are utilized for data of small dimensions. One could also successfully use DNNs in recognition tasks for small images [31].

Figure 3 depicts a four-layered fully connected neural network consisting of 18 computational units, which is also the classification model finally adopted in this study. Layer 1 is the input layer with two input nodes; Layers 2 and 3 are hidden layers, with six operation nodes per layer; Layer 4 is the output layer with four output nodes. Four classifications of input features can be implemented. The training process of NN is divided into two stages: One is to initialize the weights and bias terms of each node, and then input the feature data to obtain the output results. The second process is to dynamically adjust the parameters of each node according to the error between the output and the expected results so that the loss function value is reduced to a minimum. This dynamic adjustment is called optimization in NNs, and the optimizer used here is called Adam (Adaptive Moment Estimation) [32], which automatically adjusts the learning rate to achieve fast convergence of the loss function. Common loss functions are mean squared and mean absolute error functions for regression problems, and cross-entropy loss functions for classification problems [33]. The testing process of the NN uses the network model with the smallest loss function value of the output result and the expected result during the training process to test the sample data and count the accuracy rate.

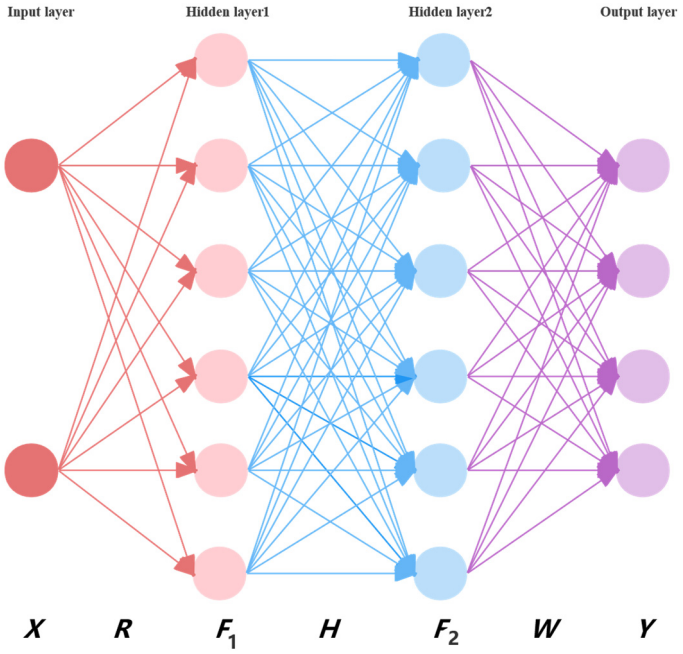

Figure 3. Schematic of the four-layered, a fully connected neural network consisting of 18 computational units used in this study.

3. Results and Discussions

3.1. FDHs of Mueller Matrix Elements for Tendon Tissues in Different States

Through the transformation process of 2D Mueller matrix elements images into MMT parameters, some detailed information can be lost that may account for the sample structure features [34]. To this end, we converted 2D Mueller matrix elements images of bovine tendon tissues firstly into FDHs, then calculated their corresponding central moments. Additional information related to the mechanical property may be obtained by analyzing the position, width, and shape of the FDHs of the Mueller matrix elements. Figure 4 shows the FDHs of 3 × 3 Mueller matrix elements for tendon tissues in four states: origin, TDO, MDO, and ODO. Here, the FDH curves of tissues in each of the four states are plotted into the same subgraph, where the blue solid lines represent MDO, the orange solid lines represent TDO, the yellow dashed lines represent ODO and the purple dashed lines represent the origin state.

It can be seen from Figure 4 that: (1) the FDHs of elements M22 and M33 are different for all the stretching states. Taking the sample without stretching (Origin) as an example, the mean values of the M22 and M33 curves are 0.16 and 0.06, respectively, meaning that the tendon tissue is highly anisotropic. In addition, the FDH curves of M33 in all four states are steeper than those of M22. However, the differences between M22 and M33 change as the stretching states change, showing that the applied external force can result in different degrees of anisotropy to the tendon tissue samples. A closer observation of Figure 4 also reveals that the FDH curves of the off-diagonal elements M12, M21, M13 and M31, which mainly present the linear dichroism property induced by fibrous scatterers, have none-zero mean values, especially for the M12 and M21 elements [35]. The none-zero values of origin sample demonstrate the existence of fibers, and the characteristic value changes with different stretchings applied show that the external force information can be extracted from the Mueller matrix elements [18,36].

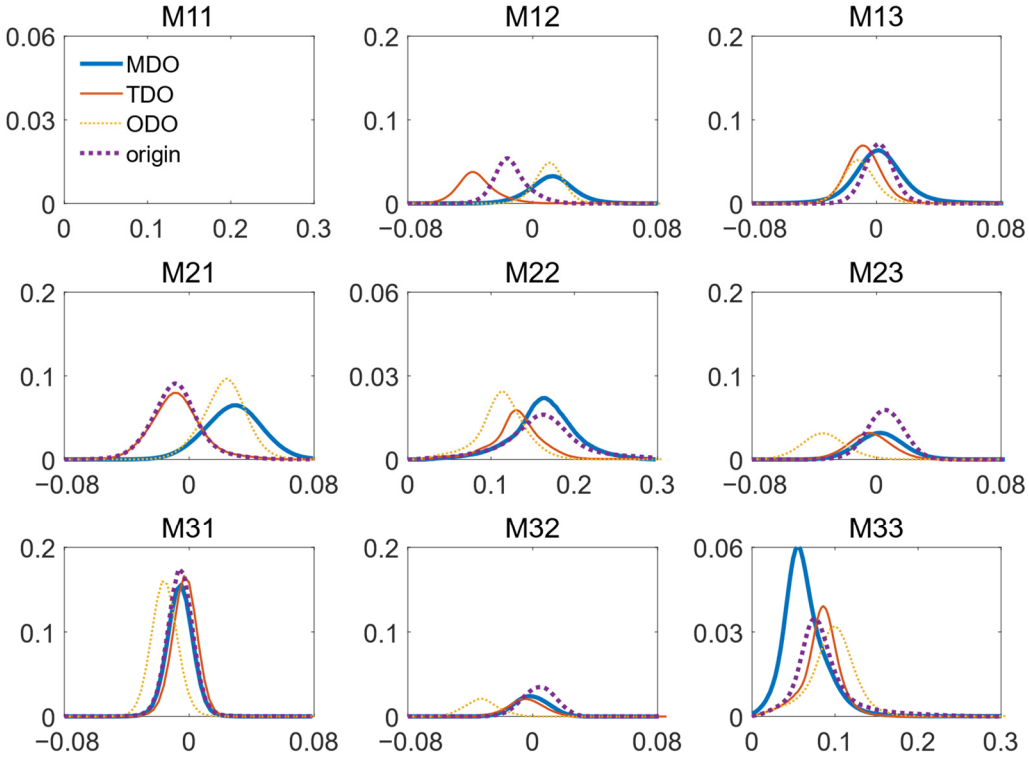

Figure 4. Frequency distribution histograms (FDHs) of 3 × 3 Mueller matrix elements for bovine tendon tissues in four states: origin, TDO, MDO and ODO. The horizontal axis is divided into 400 intervals, and the vertical axis coordinates represent the probability that the data points will fall into one of the intervals of the horizontal axis. Here, the coordinate ranges are determined according to Ref. [24].

The above conclusion illustrates that the FDHs of the Mueller matrix elements for the bovine tendon tissue samples can be significantly different when stretched by external forces. For more quantitative analysis of the relationship between the structural changes and the stretching by different external forces, we derived the MMT parameters in the next section.

3.2. MMT Parameters for Tendon Tissues in Different States

We first plot the FDH curves of the MMT parameters α_1 and t_1 for the tendon tissues in four different states in the same subplots. The α_1 and t_1 parameters of these four different states have been normalized by dividing the current value by the corresponding parameter value at the maximum absolute value of the four states. As shown in Figure 5, the blue solid lines represent the MDO state, the orange solid lines with circle markers indicate the TDO state, the yellow solid lines with triangle markers indicate the ODO state and the purple dashed lines represent the origin state.

From the FDHs of parameter α_1 shown in Figure 5a, we can see that: (1) among the four states, the FDH curve of the MDO sample has the steepest shape, which is similar to the FDH curve of origin sample; (2) the FDH curve of the ODO sample is far away from those of the other three states; and (3) the FDH curve of the TDO sample is lower than those of the other three states and has the flattest shape. From the FDHs of parameter t_1 shown in Figure 5b, it can be seen that the mean value of the FDH curves of the four states increase sequentially as TDO, ODO, origin, MDO. To statistically verify the above conclusions, we performed tensile experiments on three randomly selected bovine tendon tissue samples and calculated the central moments (I_1 to I_4 moments) of their MMT parameters α_1 and t_1.

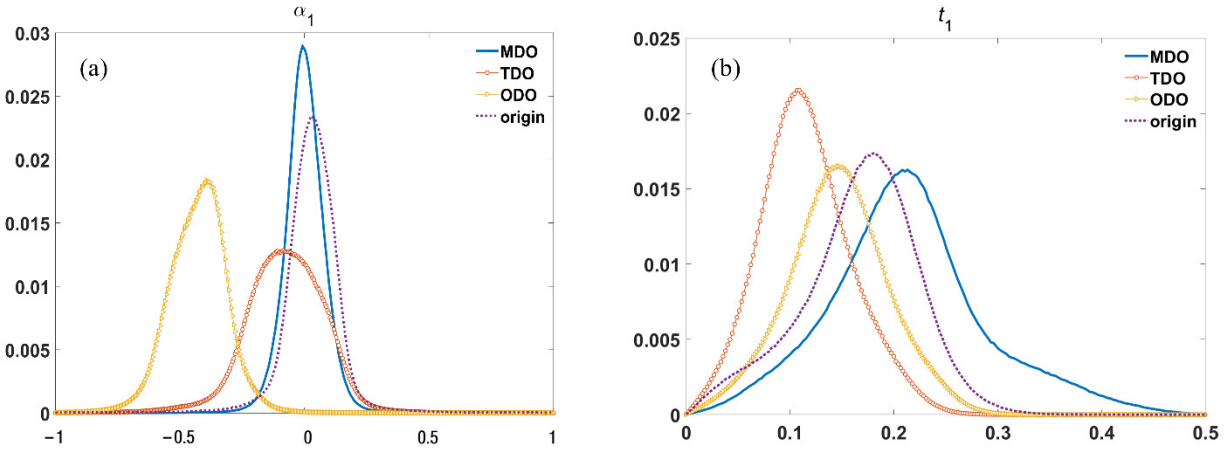

Figure 5. FDHs of MMT parameters (**a**) α_1 and (**b**) t_1 for the tendon tissues in four different states. The horizontal axis is divided into 400 intervals, and the vertical axis coordinates represent the probability that the data points fall into one of the intervals of the horizontal axis.

As shown in Table 1, for parameter α_1 in the four states of origin, TDO, MDO and ODO, the average values of the first-order moment of the three samples are 0.023, −0.003, −0.030 and −0.443, respectively. It can be seen that the first-order moment of the ODO sample is very different from those of the other three states. Because the oblique stretching makes the fiber structure very chaotic, the longitudinal or transverse stretch of its fiber structure changes are ordered, so that the general anisotropy of ODO is very different from MDO and TDO. Moreover, the average values of the second-order moment of the three samples in the origin, TDO, MDO and ODO states are 0.016, 0.173, 0.026 and 0.103, respectively. We can notice that the second-order moments of the origin and MDO samples are much smaller compared with the other two states, and the second-order moment of the TDO sample is the largest among all four states. This is because the lateral stretching makes the arrangement of the fiber structure become loose, and the closer to the center, the greater the degree of looseness, so that the range of its total anisotropy values becomes wider and the variance in the lateral stretch state becomes larger. It is also found that the mean value of the third-order moments of the ODO state is 2.123, which is larger than the mean values of third-order moments of the origin, TDO and MDO states, and the mean value of the fourth-order moments of the TDO state is 3.680, which is smaller than the mean values of fourth-order moments of the origin, ODO and MDO states.

Table 1. Central moments I_1 to I_4 of MMT parameters α_1 for bovine tendon tissue samples.

α_1	Origin			TDO			MDO			ODO		
	S_1	S_2	S_3	S_1	S_2	S_3	S_1	S_2	S_3	S_1	S_2	S_3
I_1	0.04	0.00	0.03	0.03	0.03	−0.07	−0.08	−0.01	0.00	−0.39	−0.52	−0.42
I_2	0.02	0.01	0.02	0.33	0.16	0.03	0.05	0.02	0.01	0.24	0.05	0.02
I_3	−0.35	−0.16	−0.49	−0.19	−0.02	−0.07	0.49	0.20	−0.11	1.50	3.11	1.76
I_4	7.82	5.35	16.71	1.80	2.84	6.40	5.97	5.59	18.46	4.37	18.51	19.96

As shown in Table 2, for the MMT parameter t_1 of the three tendon tissue samples in four states of origin, TDO, MDO and ODO, the average values of the first-order moment are 0.156, 0.080, 0.176 and 0.136, respectively. It shows that the first-order moment, or the expected value of the MMT parameter t_1, can be used to distinguish the stretching states of the samples. We can see from Figure 5 and Table 2 that, among the four states, the tendon tissues in the TDO state have the smallest mean t_1 values, while the ones in the MDO states have the largest mean t_1 values. The reason for this is that stretching the tendon tissue along the direction of the fibers leads to them being arranged more orderly and tightly,

thus strengthening the anisotropy. Meanwhile, stretching the tendon tissue perpendicular to the direction of the fibers results in them spreading apart and weakening the anisotropy.

Table 2. Central moments I_1 to I_4 of MMT parameters t_1 for bovine tendon tissue samples.

t_1	Origin			TDO			MDO			ODO		
	S_1	S_2	S_3	S_1	S_2	S_3	S_1	S_2	S_3	S_1	S_2	S_3
I_1	0.10	0.20	0.17	0.03	0.09	0.12	0.08	0.24	0.21	0.05	0.21	0.15
I_2	0.00	0.00	0.00	0.00	0.00	0.00	0.00	0.01	0.01	0.00	0.01	0.00
I_3	0.13	−0.23	−0.31	1.43	0.84	0.33	0.19	−0.17	0.42	0.70	−0.15	0.03
I_4	2.93	3.23	3.28	7.95	4.41	3.20	3.31	2.78	3.54	3.82	3.07	3.08

Moreover, it can be noticed from Table 2 that the second-order moment I_2 values of all the samples are very close to 0, which results from the very small I_1 values. The third and fourth-order moments I_3 and I_4 of the parameter t_1 are largest in TDO, and the difference in the remaining three states is not obvious because the values of anisotropy in the TDO state are generally the smallest.

In summary, the analysis in this section confirms that for the MMT parameter α_1, its central moments can be used to distinguish among different stretching states of tendon tissues. For the MMT parameter t_1, its first-order moment can be used to distinguish between TDO and MDO states, and its third and fourth-order moments can be used to distinguish between TDO and other states.

3.3. Separation of Tendon Tissues in Different States Using NN Classifiers

The above section shows that, there are several indicators of the MMT parameters α_1 and t_1 that could distinguish among the four stretching states of tendon tissues. However, to reduce the complexity of the NN and improve the classification speed of the model, here we selected two of them for input into the model. The reason for this is that the first-order moment of the parameter t_1 can discriminate the samples in the TDO and MDO states, and the first-order moment of the parameter α_1 can discriminate the samples in the ODO state. Thus, in this section, the NN has two input nodes, one is I_1 of parameter t_1 indicated as x_1 in Equation (8), and the second input node is I_1 of parameter α_1 indicated as x_2 in Equation (8). For testing, the parameters x_1 and x_2 have been normalized by subtracting the minimum value from the current value and dividing by the difference between the maximum and minimum values. The NN also has four output nodes corresponding to four stretching states. Training tests showed that when there are two hidden layers with six nodes in each layer, as illustrated in Figure 3, a good classification can be achieved by the NN model. We use vectors to describe the entire network. The two nodes of the input layer are represented as Equation (8):

$$X = [x_1 \; x_2]^{\mathrm{T}} \tag{8}$$

The weights R on the connection line between the input layer and the first hidden layer are shown in Equation (9), where r_{11} represents the weights on the line from the first neuron of the input layer to the first neuron of the first hidden layer, and so on for the rest of the parameters:

$$R = \begin{bmatrix} r_{11} & r_{12} & r_{13} & r_{14} & r_{15} & r_{16} \\ r_{21} & r_{22} & r_{23} & r_{24} & r_{25} & r_{26} \end{bmatrix}^{\mathrm{T}} \tag{9}$$

Then, the data received by each node of the first hidden layer are $R \times X$, and on this basis, the bias term B_1 of each node is added as Equation (10):

$$B_1 = [b_{11} \quad b_{12} \quad b_{13} \quad b_{14} \quad b_{15} \quad b_{16} \;]^{\mathrm{T}} \tag{10}$$

After the activation of function *Leaky_Relu*, the output F_1 of the first hidden layer is obtained as Equation (11):

$$F_1 = leaky\_relu(R \times X + B_1) = leaky\_relu\left(\begin{bmatrix} r_{11} \times x_1 + r_{21} \times x_2 + b_{11} \\ r_{12} \times x_1 + r_{22} \times x_2 + b_{12} \\ r_{13} \times x_1 + r_{23} \times x_2 + b_{13} \\ r_{14} \times x_1 + r_{24} \times x_2 + b_{14} \\ r_{15} \times x_1 + r_{25} \times x_2 + b_{15} \\ r_{16} \times x_1 + r_{26} \times x_2 + b_{16} \end{bmatrix}\right) \quad (11)$$

Similarly, if the weight on the connection line between the first hidden layer and the second hidden layer is H (six rows and six columns), the data received by the nodes of the second hidden layer are $H \times F_1$, and the bias term B_2 (six rows and one column) of each node will be added on this basis. Then, the output F_2 of the second hidden layer (six rows and one column) will be obtained through the activation function *Leaky_Relu*, shown in Equation (12):

$$F_2 = leaky\_relu(H \times F_1 + B_2) \quad (12)$$

The weight on the connection line between the second hidden layer and the output layer is W (four rows and six columns). Then, the data received by each node of the output layer are $W \times F_2$. On this basis, the bias term B_3 (four rows and one column) of each node is added, and then the final output Y (four rows and one column) is obtained by the activation function *Leaky_Relu*, shown in Equation (13):

$$Y = leaky\_relu(W \times F_2 + B_3) \quad (13)$$

Therefore, the entire network can be represented by vectors as Equation (14):

$$Y = leaky\_relu(W \times leaky\_relu(H \times leaky\_relu(R \times X + B_1) + B_2) + B_3) \quad (14)$$

The whole network delivers y_1, y_2, y_3 and y_4 in four output nodes after passing through the model. Labels 0, 1, 2 and 3 indicate the four stretching states of MDO, ODO, origin and TDO, respectively [37]. The output result is compared with the label by the cross-entropy loss function. To reduce the loss, we use the Adam optimizer to iteratively update the weights and biases of the NN. When the loss converges to a minimum, the model training ends [38]. The purpose of NN training is to solve for the weights R, H and W and bias B_1, B_2 and B_3 of each node.

As shown in Figure 6, for the classification model testing, we adopted data enhancement methods such as random cropping and random rotation to the parameters α_1 and t_1 images of each tendon tissue sample. The 24 parameter images were enhanced to 2848 images (1424 blocks for each parameter) to improve the generalization ability of the model [39]. The first-order moment I_1 values of the small blocks were calculated to obtain x_1 and x_2. Finally, we acquired 1424 sets of input features x_1 and x_2, of which the training set had 1140 groups and the test set had 284 groups. The number of groups of input features in the four states is equal in both the training set and the test set. We plot all the data in the four states in a graph, and it is obvious that there are significant differences in the data distribution of these four states, such as the data of ODO are mainly distributed in the lower left corner of the graph, the data of TDO are mainly distributed in the lower right corner and the data of MDO are mainly distributed in the upper right corner, which is the primary condition for using neural networks to distinguish the four states.

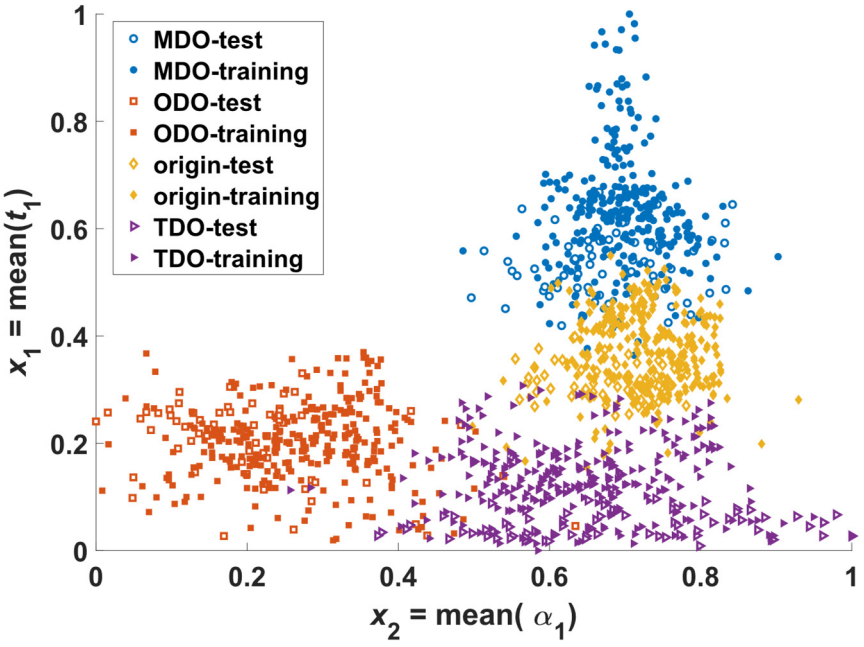

Figure 6. Scatter plot of training and test set data.

We randomly scrambled the training set data. Among them, every 100 sets of data are regarded as a batch to be inputted to the network model. Here, a training cycle epoch has a total of 11 batches. The learning rate is set to 0.01; when trained for 300 cycles, the model's loss converges to a minimum of 0.02. At this time, the weights R, H and W and bias B_1, B_2 and B_3 of each node are shown in Tables 3 and 4.

Table 3. Weights and biases of each node of the classification model. R (6 rows and 2 columns), H (6 rows and 6 columns), W (4 rows and 6 columns).

R		H						W					
−0.858	2.267	1.933	−2.096	2.455	1.813	1.863	0.724						
1.829	−3.686	1.103	2.323	−2.277	0.248	−1.640	−1.023						
1.270	2.833	−0.436	0.946	3.476	1.090	1.991	0.494	2.348	−0.838	1.459	−0.292	−6.215	−1.836
0.217	1.851	0.165	1.112	0.052	−0.331	−0.670	0.034	−0.630	1.462	−1.537	−0.884	2.807	−0.937
1.922	0.926	−1.955	−0.449	−1.472	−4.153	0.440	−2.365	0.835	−3.253	1.144	−2.456	1.596	1.355
−0.143	0.083	−2.326	1.494	1.210	−2.034	0.850	0.132	−3.301	1.408	1.408	1.732	−0.834	0.808

Table 4. Weights and biases of each node of the classification model. B_1 (6 rows and 1 column), B_2 (6 rows and 1 column), B_3 (4 rows and 1 column).

B_1	B_2	B_3
−0.454	0.186	
0.678	1.547	
−0.901	−0.648	−0.462
−1.058	−0.381	1.405
−0.636	2.597	−0.066
−0.815	−0.229	0.065

After the network model parameters are trained, to show the classification effect of the NN model, it is necessary to quantitatively evaluate its classification accuracy. When the accuracy of a classification method is evaluated, the main indicators include:

(1) Classification accuracy, which is the ratio of the correct classification quantity to the total quantity;

(2) Confusion matrix, which is mainly used to compare the difference between the classification result and the real situation. In the confusion matrix, the number of misclassified samples is distributed on the non-diagonal line, while the number of correctly classified samples is distributed on the diagonal line, so it is convenient to view the confusion of multiple categories with the help of the confusion matrix [40];

(3) *kappa* Coefficient, which is an indicator for testing consistency. The so-called consistency refers to whether the model prediction results and the actual classification results are consistent, and its calculation method is shown in Equation (15) [41], where N represents the sum of all the elements of the confusion matrix, $\sum_{i=1}^{n} x_{ii}$ represents the sum of the diagonal elements of the confusion matrix and $\sum_{i=1}^{n} x_{i*}x_{*i}$ represents the product of the sum of row elements and column elements of the confusion matrix.

$$kappa = \frac{N* \sum_{i=1}^{n} x_{ii} - \sum_{i=1}^{n} x_{i*}x_{*i}}{N^2 - \sum_{i=1}^{n} x_{i*}x_{*i}} \quad (15)$$

Here, we divided the 284 groups of test data sets into four sub-sets according to the four labels of 0, 1, 2 and 3. Thus, each test set has 71 groups of data. The four test sets were inputted into the model separately, and the model classification results were compared with the labels to obtain the confusion matrix as shown in Table 5.

Table 5. Confusion matrix.

Real Predict	0 (MDO)	1 (ODO)	2 (Origin)	3 (TDO)
0(MDO)	70	1	0	0
1(ODO)	0	71	0	0
2(origin)	1	0	69	1
3(TDO)	0	3	0	68

From the confusion matrix, the classification accuracy of MDO, ODO, origin and TDO can be calculated to be 99%, 100%, 97% and 96%, respectively, and the total classification accuracy is 98%. The coefficient is 0.972, indicating that the classification results of the NN model are in good agreement with the actual classification [42].

The above results show that the combination of the NN model and polarization parameters can be applied to the classification prediction of the stretching states of tendon tissues, thus demonstrating the great application potential of polarization parameters in the field of biomechanics.

The Mueller matrix is rich in microstructural information, and we find that the different force states have different effects on each matrix element. Among them, M12, M13, M31 and M21 matrix elements are mainly sensitive to changes in linear dichroism, and M22 and M33 mainly reflect the linear depolarization of the samples. The MMT parameters t_1 (total anisotropy) and α_1 (orientation of the general anisotropy), consisting of M22, M33, M23 and M32 elements, were found to be sensitive to the differentiation of different force states. Stretching the tendon tissue along the direction of the fibers resulted in a more ordered and tighter arrangement, thus enhancing its anisotropy. Meanwhile, stretching the tendon tissues perpendicular to the direction of the fibers causes them to disperse and weakens their anisotropy. Oblique stretching exists in both cases. Among the four states, the TDO state has the smallest tendon tissue t_1, the MDO state has the largest tendon tissue t_1 and the ODO and origin have a close t_1. For α_1, which represents the direction of anisotropy, ODO and the other three states have a clear distinction. It should be noticed that different types of bovine tendon tissues can generate different quantitative Mueller matrix parameter values. However, according to the analysis above, the relationship between the stretching states and the Mueller matrix parameters would not be changed. The four states can still be differentiated with different tendon tissue samples.

4. Conclusions

In this work, to quantitatively evaluate the mechanical properties of tendon tissues, we measured the 3×3 backscattering Mueller matrix of bovine tendon tissue with different stretching of external forces by using a device based on a polarization camera. Then we performed FDH processing on the Mueller matrix elements and an MMT parameters analysis. The studies revealed that the MMT parameters α_1 and t_1 can be used to distinguish tendon tissues in different stretching states. The central moments of the MMT parameter α_1 can be used to distinguish the different stretching states of the tendon tissue. For the MMT parameter t_1, its first-order moments can be used to distinguish between TDO and MDO states, and its third and fourth-order moments can be used to distinguish between TDO and other states. In order to make better use of the MMT parameters to quickly and accurately distinguish the tendon tissue samples with different external forces, we designed a four-layered classification neural network model. After multiple pieces of training, the value of the cross-entropy loss function was reduced to the minimum, and the trained network was then used as the final classification model to achieve a classification accuracy of 98%. The results shown in this study demonstrated that the polarization-camera-based Mueller matrix polarimeter can be used for rapid measurement of tissue samples. Combined with quantitative analysis parameters and a NN, this method is beneficial to future practical applications such as biomechanics monitoring.

Author Contributions: Conceptualization, C.M. and H.H.; data curation, C.M. and C.S.; methodology, C.M. and C.S.; supervision, H.H., C.H. and H.M.; writing—original draft, C.M. and C.S.; writing—review and editing, H.H. and C.H. All authors have read and agreed to the published version of the manuscript.

Funding: This research was funded by Shenzhen Key Fundamental Research Project (No. JCYJ20210324120012035).

Institutional Review Board Statement: Not applicable.

Informed Consent Statement: Not applicable.

Data Availability Statement: The data presented in this study are available on request from the corresponding author.

Conflicts of Interest: The authors declare no conflict of interest.

References

1. Tekieli, M.; De Santis, S.; de Felice, G.; Kwiecień, A.; Roscini, F. Application of Digital Image Correlation to Composite Reinforcements Testing. *Compos. Struct.* **2017**, *160*, 670–688. [CrossRef]
2. Liu, C.; Dai, Y.T.; Dai, M.L.; Liu, X.; Zhu, C.; Shao, X.; He, X. Deformation measurement by two-dimensional multi-camera full-field digital image correlation. *Acta Opt. Sin.* **2016**, *36*, 97–112.
3. Shunqing, Z.; Chenjia, G.A.O.; Long, Z. The Development and Latest Applications of Digital Image Correlation in Stress and Strain Measurement. *Imaging Sci. Photochem.* **2017**, *35*, 193.
4. Innocenti, B. Chapter 2—Mechanical Properties of Biological Tissues. In *Human Orthopaedic Biomechanics*; Academic Press: Cambridge, MA, USA, 2022; pp. 9–24.
5. Pan, B.; Wang, B. Research Progress in Digital Volume Correlation Method. *Chin. Sci. Bull.* **2017**, *62*, 1671–1681. [CrossRef]
6. Huňady, R.; Hagara, M. A New Procedure of Modal Parameter Estimation for High-Speed Digital Image Correlation. *Mech. Syst. Signal Process.* **2017**, *93*, 66–79. [CrossRef]
7. Kennedy, B.F.; Wijesinghe, P.; Sampson, D.D. The Emergence of Optical Elastography in Biomedicine. *Nat. Photonics* **2017**, *11*, 215–221. [CrossRef]
8. Konarski, W.; Poboży, T.; Kotela, A.; Hordowicz, M.; Poboży, K. Ultrasound in the Differential Diagnosis of Medial Epicondylal gia and Medial Elbow Pain-Imaging Findings and Narrative Literature Review. *Healthcare* **2022**, *10*, 1529. [CrossRef]
9. He, H.; Liao, R.; Zeng, N.; Li, P.; Chen, Z.; Liu, X.; Ma, H. Mueller Matrix Polarimetry—An Emerging New Tool for Characterizing the Microstructural Feature of Complex Biological Specimen. *J. Light. Technol.* **2019**, *37*, 2534–2548. [CrossRef]
10. Shen, Y.; Chen, B.; He, C.; He, H.; Guo, J.; Wu, J.; Elson, D.S.; Ma, H. Polarization Aberrations in High-Numerical-Aperture Lens Systems and Their Effects on Vectorial-Information Sensing. *Remote Sens.* **2022**, *14*, 1932. [CrossRef]
11. Azzam, R.M. Photopolarimetric Measurement of the Mueller Matrix by Fourier Analysis of a Single Detected Signal. *Opt. Lett.* **1978**, *2*, 148. [CrossRef]

12. He, C.; He, H.; Chang, J.; Chen, B.; Ma, H.; Booth, M.J. Polarisation Optics for Biomedical and Clinical Applications: A Review. *Light Sci. Appl.* **2021**, *10*, 194. [CrossRef] [PubMed]
13. Huang, T.; Meng, R.; Qi, J.; Liu, Y.; Wang, X.; Chen, Y.; Liao, R.; Ma, H. Fast Mueller Matrix Microscope Based on Dual DoFP Polarimeters. *Opt. Lett.* **2021**, *46*, 1676. [CrossRef] [PubMed]
14. Zhou, J.; He, H.; Chen, Z.; Wang, Y.; Ma, H. Modulus Design Multiwavelength Polarization Microscope for Transmission Mueller Matrix Imaging. *J. Biomed. Opt.* **2018**, *23*, 1. [CrossRef] [PubMed]
15. Chen, B.; Lan, Y.; Zhai, H.; Deng, L.; He, H.; Mao, H.; Ma, H. Comparative Study of Modified Mueller Matrix Transformation and Polar Decomposition Parameters for Transmission and Backscattering Tissue Polarimetries. *Appl. Sci.* **2021**, *11*, 10416. [CrossRef]
16. Liu, T.; Sun, T.; He, H.; Liu, S.; Dong, Y.; Wu, J.; Ma, H. Comparative Study of the Imaging Contrasts of Mueller Matrix Derived Parameters between Transmission and Backscattering Polarimetry. *Biomed. Opt. Express* **2018**, *9*, 4413. [CrossRef]
17. He, H.; Sun, M.; Zeng, N.; Du, E.; Liu, S.; Guo, Y.; Wu, J.; He, Y.; Ma, H. Mapping Local Orientation of Aligned Fibrous Scatterers for Cancerous Tissues Using Backscattering Mueller Matrix Imaging. *J. Biomed. Opt.* **2014**, *19*, 106007. [CrossRef]
18. Sun, T.; Liu, T.; He, H.; Wu, J.; Ma, H. Distinguishing anisotropy orientations originated from scattering and birefringence of turbid media using Mueller matrix derived parameters. *Opt. Lett.* **2018**, *43*, 4092–4095. [CrossRef]
19. Qi, J.; Elson, D.S. Mueller polarimetric imaging for surgical and diagnostic applications: A review. *J. Biophotonics* **2017**, *10*, 950–982. [CrossRef]
20. He, H.; Zeng, N.; Du, E.; Guo, Y.; Li, D.; Liao, R.; He, Y.; Ma, H. Two-Dimensional and Surface Backscattering Mueller Matrices of Anisotropic Sphere-Cylinder Scattering Media: A Quantitative Study of Influence from Fibrous Scatterers. *J. Biomed. Opt.* **2013**, *18*, 046002. [CrossRef]
21. Li, P.; Dong, Y.; Wan, J.; He, H.; Tariq, A.; Ma, H. Polaromics: Deriving polarization parameters from a Mueller matrix for quantitative characterization of biomedical specimen. *J. Phys. D Appl. Phys.* **2021**, *55*, 034002. [CrossRef]
22. Chen, B.; Li, W.; He, H.; He, C.; Guo, J.; Shen, Y.; Liu, S.; Sun, T.; Wu, J.; Ma, H. Analysis and Calibration of Linear Birefringence Orientation Parameters Derived from Mueller Matrix for Multi-Layered Tissues. *Opt. Lasers Eng.* **2021**, *146*, 106690. [CrossRef]
23. Alali, S.; Vitkin, I.A. Polarized light imaging in biomedicine: Emerging Mueller matrix methodologies for bulk tissue assessment. *J. Biomed. Opt.* **2015**, *20*, 061104. [CrossRef]
24. He, C.; He, H.; Li, X.; Chang, J.; Wang, Y.; Liu, S.; Zeng, N.; He, Y.; Ma, H. Quantitatively Differentiating Microstructures of Tissues by Frequency Distributions of Mueller Matrix Images. *J. Biomed. Opt.* **2015**, *20*, 105009. [CrossRef] [PubMed]
25. Dong, Y.; He, H.; Sheng, W.; Wu, J.; Ma, H. A quantitative and non-contact technique to characterise microstructural variations of skin tissues during photo-damaging process based on Mueller matrix polarimetry. *Sci. Rep.* **2017**, *7*, 14702. [CrossRef] [PubMed]
26. Grimmett, G.; Stirzaker, D. *Probability and Random Processes*; Oxford University Press: Oxford, UK, 2001.
27. Ushenko, V.A.; Dubolazov, O.V.; Karachevtsev, A.O. Two Wavelength Mueller Matrix Reconstruction of Blood Plasma Films Polycrystalline Structure in Diagnostics of Breast Cancer. *Appl. Opt.* **2014**, *53*, B128. [CrossRef] [PubMed]
28. Aulestia, P.S.; Talahua, J.S.; Andaluz, V.H.; Benalcázar, M.E. Real-Time Face Detection Using Artificial Neural Networks. In Proceedings of the Artificial Neural Networks and Machine Learning—ICANN, Alghero, Italy, 11–14 September 2017; Springer: Cham, Switzerland, 2017; pp. 590–599.
29. Cavalin, P.; Oliveira, L.S. A Review of Texture Classification Methods and Databases. In Proceedings of the 2017 30th SIBGRAPI Coference on Graphics, Patterns and Images Tutorials (SIBGRAPI-T), Niteroi, Brazil, 17–18 October 2017; pp. 1–8.
30. Bera, K.; Schalper, K.A.; Rimm, D.L.; Velcheti, V.; Madabhushi, A. Artificial Intelligence in Digital Pathology—New Tools for Diagnosis and Precision Oncology. *Nat. Rev. Clin. Oncol.* **2019**, *16*, 703–715. [CrossRef]
31. Otter, D.W.; Medina, J.R.; Kalita, J.K. A Survey of the Usages of Deep Learning for Natural Language Processing. *IEEE Trans. Neural Netw. Learn. Syst.* **2021**, *32*, 604–624. [CrossRef]
32. Dong, Y.; Wan, J.; Wang, X.; Xue, J.-H.; Zou, J.; He, H.; Li, P.; Hou, A.; Ma, H. A Polarization-Imaging-Based Machine Learning Framework for Quantitative Pathological Diagnosis of Cervical Precancerous Lesions. *IEEE Trans. Med. Imaging* **2021**, *40*, 3728–3738. [CrossRef]
33. He, K.; Zhang, X.; Ren, S.; Sun, J. Deep Residual Learning for Image Recognition. In Proceedings of the 2016 IEEE Conference on Computer Vision and Pattern Recognition (CVPR), Las Vegas, NV, USA, 27–30 June 2016; pp. 770–778.
34. He, C.; Chang, J.; Hu, Q.; Wang, J.; Antonello, J.; He, H.; Liu, S.; Lin, J.; Dai, B.; Elson, D.S.; et al. Complex Vectorial Optics through Gradient Index Lens Cascades. *Nat. Commun.* **2019**, *10*, 4264. [CrossRef]
35. He, C.; Chang, J.; Salter, S.P.; Shen, Y.; Dai, B.; Li, P.; Jin, Y.; Thodika, S.C.; Li, M.; Tariq, A.; et al. Revealing complex optical phenomena through vectorial metrics. *Adv. Photon.* **2022**, *4*, 026001. [CrossRef]
36. Shen, Y.; Huang, R.; He, H.; Liu, S.; Dong, Y.; Wu, J.; Ma, H. Comparative study of the influence of imaging resolution on linear retardance parameters derived from the Mueller matrix. *Biomed. Opt. Express* **2021**, *12*, 211–225. [CrossRef] [PubMed]
37. Uijlings, J.R.R.; van de Sande, K.E.A.; Gevers, T.; Smeulders, A.W.M. Selective Search for Object Recognition. *Int. J. Comput. Vis.* **2013**, *104*, 154–171. [CrossRef]
38. Rivenson, Y.; Wang, H.; Wei, Z.; de Haan, K.; Zhang, Y.; Wu, Y.; Günaydın, H.; Zuckerman, J.E.; Chong, T.; Sisk, A.E.; et al. Virtual Histological Staining of Unlabelled Tissue-Autofluorescence Images via Deep Learning. *Nat. Biomed. Eng.* **2019**, *3*, 466–477. [CrossRef] [PubMed]

39. Cuingnet, R.; Rosso, C.; Chupin, M.; Lehéricy, S.; Dormont, D.; Benali, H.; Samson, Y.; Colliot, O. Spatial Regularization of SVM for the Detection of Diffusion Alterations Associated with Stroke Outcome. *Med. Image Anal.* **2011**, *15*, 729–737. [CrossRef] [PubMed]
40. Youngentob, S.L.; Markert, L.M.; Mozell, M.M.; Hornung, D.E. A Method for Establishing a Five Odorant Identification Confusion Matrix Task in Rats. *Physiol. Behav.* **1990**, *47*, 1053–1059. [CrossRef]
41. Tang, W.; Hu, J.; Zhang, H.; Wu, P.; He, H. Kappa Coefficient: A Popular Measure of Rater Agreement. *Shanghai Arch. Psychiatry* **2015**, *27*, 62–67.
42. Huang, J.; Rathod, V.; Sun, C.; Zhu, M.; Korattikara, A.; Fathi, A.; Fischer, I.; Wojna, Z.; Song, Y.; Guadarrama, S.; et al. Speed/Accuracy Trade-Offs for Modern Convolutional Object Detectors. In Proceedings of the 2017 IEEE Conference on Computer Vision and Pattern Recognition (CVPR), Honolulu, HI, USA, 21–26 July 2017; pp. 3296–3297.